Electronic Structure of Oxygen Interstitial Defects in Amorphous In-Ga-Zn-O Semiconductors and Implications for Device Behavior

W. H. Han, Young Jun Oh, and K. J. Chang*

Department of Physics, Korea Advanced Institute of Science and Technology, Daejeon 305-701, Republic of Korea

Ji-Sang Park

National Renewable Energy Laboratory, Golden, Colorado 80401, USA

(Received 10 February 2015; published 16 April 2015)

We investigate the atomic and electronic properties of O interstitial defects in amorphous In-Ga-Zn-O (*a*-IGZO) through density-functional calculations. We find that an O interstitial forms a dimer with a host O atom in its neutral state, but the O—O dimer bond is easily broken upon electron capture. When bond-breaking relaxations take place, the antibonding defect level of the dimer is significantly lowered from the conduction band toward the valence-band edge, making it energetically more favorable for the dimer to capture two electrons. With the hybrid functional for the exchange-correlation energy, the agreement of the energy barrier for two-electron capture with an experiment is greatly improved. The implication of the results is that O interstitials act as electron traps for the Fermi level close to the conduction-band edge; thus, excess O atoms can be the origin of positive shifts of threshold voltage observed under positive-bias stress in *a*-IGZO thin-film transistors. On the other hand, under light-illumination or negative-bias stress, which lower the Fermi level to the valence-band edge, the original dimer configuration is recovered by capturing hole carriers without any energy barrier, and the stability of current-voltage characteristics is restored.

DOI: 10.1103/PhysRevApplied.3.044008

I. INTRODUCTION

Amorphous oxide semiconductors such as amorphous indium-gallium-zinc oxide (*a*-IGZO) attract much attention because of the large band gap, unintentional *n*-type conductivity, and uniformity in film growth. Oxide-based thin-film transistors (TFTs), in which *a*-IGZO is used as an active channel, show superior performance compared with conventional Si-based TFTs [1]. The conduction band of *a*-IGZO is characterized by the In *s* orbital. Thus, *n*-type conductivity is insensitive to disorder, leading to field-effect mobility higher by more than a factor of 10 than that of covalently bonded amorphous Si [2]. Although *a*-IGZO is considered a promising material for high-performance flexible electronic devices, this material still suffers from a high density of defects which cause the instability of threshold voltage (V_{th}) under various stress conditions.

There have been extensive studies on the influence of gate voltage, gate dielectrics, light illumination, temperature, passivation, and ambient environment on the characteristics of *a*-IGZO TFTs. Under negative-bias illumination stress (NBIS), *a*-IGZO TFTs exhibit large negative shifts of V_{th} up to about −18 V [3,4]. The negative shift of V_{th} is related to the charge trapping of hole carriers produced by light illumination [5]. In theoretical studies [6,7], O-vacancy defects have been shown to act as charge traps and have been suggested to be responsible for the NBIS instability. Other models have been recently proposed, based on a defect complex consisting of an O interstitial and hydrogen [8] and the lattice instability induced by a hole carrier [9]. On the other hand, when *a*-IGZO TFTs are under positive-bias stress (PBS), the so-called PBS instability takes place, with positive shifts of V_{th}, while devices usually exhibit good stability under negative-bias stress [10–13]. In contrast to the NBIS instability, the PBS instability is thought to be caused by electron traps in gate dielectrics and/or the *a*-IGZO–dielectrics interface [10,12,14] and by adsorption of oxygen molecules from the ambient atmosphere [11,15]. Defect creation in bulk *a*-IGZO or at interface was suggested as another possible origin of the PBS instability [13]. Numerous experiments show that O-related defects such as the O vacancy and O interstitial play an important role in device instability. The stability of oxide TFTs is very sensitive to the oxygen content in *a*-IGZO: an O-rich device is stable against negative-bias stress, whereas an O-deficient device is stable against positive-bias stress [16]. The creation of subgap states has been observed under the NBIS condition [17]. The NBIS instability has been improved by annealing under a high-pressure oxygen ambient, which effectively reduces active O-vacancy defects [18], thus, providing support for the mechanism

*kjchang@kaist.ac.kr

involving O-vacancy defects. However, no microscopic studies have been done to understand the mechanism for the PBS instability, although several conjectures have been given.

First-principles calculations are widely used to study the electronic properties of defects and impurities in semiconductors. In the approach which relies on the local density approximation or the generalized-gradient approximation (GGA) within the density-functional theory (DFT), the band gap is severely underestimated, causing large errors in the formation energies and transition levels of defects [19]. On the other hand, DFT calculations with a hybrid functional [20,21] have shown great improvements in the band gap as well as defect transition levels. In the present work, we perform hybrid functional calculations to investigate the electronic and optical properties of O interstitial defects in *a*-IGZO and the role of these defects in the PBS instability observed in *a*-IGZO thin-film transistors. In the amorphous phase, although the band-edge states are not generally well defined, we determine accurately the defect transition levels with respect to the valence-band edge by using the logarithmic inverse participation ratio which describes the degree of localization for the eigenstates. With the improvement of the band gap and defect levels, the energy barrier for the capture process of electrons by the O interstitial is in good agreement with the experiment, and the optical excitation of the charged defect is accurately described.

II. CALCULATION METHOD

For the composition ratio of $\mathrm{In:Ga:Zn:O} = 1:1:1:4$, we generate the amorphous model for *a*-IGZO through melt-and-quench *ab initio* molecular dynamics (MD) simulations, which use the GGA functional for the exchange-correlation potential [22] and the projector-augmented wave potentials [23], as implemented in the VASP code [24]. In a supercell containing 84 host atoms, we use a plane-wave basis to expand the wave functions with an energy cutoff of 400 eV and a k-point set generated by the $3\times3\times3$ Monkhorst-Pack mesh for Brillouin-zone integration. For O-related defects, such as O vacancy (V_{O}) and O interstitial (O_i), the ionic coordinates are fully optimized until the residual forces are less than 0.05 eV/Å. The amorphous structure exhibits the coordination numbers and metal—oxygen bond lengths in good agreement with extended x-ray absorption fine-structure measurements [25,26]. The details of the MD approach and the structural characteristics of the amorphous phase are given elsewhere [6].

Since the GGA calculations overestimate the positions of metal d bands, we include the on-site Coulomb correlation (U), which is described by a Hubbard-like term [27]. The on-site Coulomb correlation reduces the p-d hybridization; thus, the metal d bands are lowered. With the parameters of $U = 7$, 8, and 8 eV for the In 4d, Ga 3d, and Zn 3d orbitals, respectively, the positions of the metal d bands are well reproduced, compared with photoelectron spectroscopy measurements [28,29]. Although the band gap is improved by a downward shift of the valence-band edge, the GGA + U band gap, which is estimated to be 2.07 eV for pristine *a*-IGZO, is still underestimated. To get more reliable defect levels in the band gap, we employ the hybrid functional of Heyd, Scuseria, and Ernzerhof (HSE) for the exchange-correlation potential [20,21]. With the screening parameter of $\omega = 0.2$ Å^{-1} and the mixing fraction of $\alpha = 0.22$, which represents the mixing ratio of the exact short-range Hartree-Fock exchange, we obtain the band gap of 3.18 eV, close to the measured value of about 3.2 eV [30]. In this case, we take the on-site Coulomb parameters of $U = 3.5$, 4.0, and 4.0 eV for the In, Ga, and Zn d orbitals, respectively, to reproduce the measured values for the metal d bands.

The formation energy of an O_i defect in charge state q is expressed as

$$\Omega(\mathrm{O}_i^q) = E_{\mathrm{tot}}(\mathrm{O}_i^q) - E_{\mathrm{tot}}^0 - \mu_{\mathrm{O}} + q(\epsilon_{\mathrm{VBM}} + E_F), \quad (1)$$

where $E_{\mathrm{tot}}(\mathrm{O}_i^q)$ and E_{tot}^0 are the total energies of supercells with and without the defect, respectively, and E_F is the Fermi energy with respect to the valence-band maximum (VBM) ϵ_{VBM}. The oxygen chemical potential μ_{O} is determined from an isolated O_2 molecule and estimated to be −4.96 and −6.81 eV under the extreme O-rich condition by the GGA + U and HSE calculations, respectively. Since *a*-IGZO has tail states near the band edges due to structural disorder and defects, it is difficult to define the VBM and conduction-band minimum (CBM) states. To determine the band-edge states, we calculate the normalized logarithm of the inverse participation ratio (LIPR) [31],

$$\mathrm{LIPR}(E) = \frac{\ln \mathcal{P}(E)}{\ln(N)}, \quad (2)$$

where the inverse participation ratio is defined as $\mathcal{P}(E) = \sum_{i=1}^{N} |\Psi_E(\mathbf{r}_i)|^4$, $\Psi_E(\mathbf{r}_i)$ is the wave-function amplitude at the ith atom, and N is the total number of atoms. The LIPR measures the degree of localization: it is close to −1 for an extended state, whereas it increases up to 0 as the energy state becomes localized. The LIPR value varies with the energy level. The valence-band-edge state is characterized by the O 2p orbitals. Depending on the energy level, the charge density is well distributed over the O atoms or localized at some particular O atoms. Thus, we examine the charge distributions of the states near the band edges and find that the LIPR value of −0.7 is suitable for the criteria of extended and localized states. We note that our main results are not altered even if the LIPR criteria vary by a small amount.

III. RESULTS AND DISCUSSION

A. Atomic and electronic structure of the O interstitial

We generate 21 different configurations of an O_i defect by inserting a guest O atom in various interstitial positions in *a*-IGZO. In the neutral state, the O_i defect forms an O—O dimer with one of the host O atoms in the most stable configuration [Fig. 1(a)]. This dimer structure is very similar to that of a split-interstitial complex, which was suggested to be the stable O_i defect in crystalline IGZO and ZnO [32–34]. The O—O bond lengths range from 1.48 to 1.56 Å, with the average value of 1.51 Å, which is larger than that of an isolated O_2 molecule (1.21 Å) due to interactions with the surrounding metal ions. In the 2− charge state, the O—O dimer bond is broken [Fig. 1(b)]. Since the antibonding state of the O—O dimer is occupied, the distance between the host and guest O atoms significantly increases to 2.60–2.72 Å, resulting in the average O—O distance of 2.69 Å. Because of large structural relaxations, the guest O atom is directly bonded to its nearest metal ions. The atomic structure of the broken O—O dimer is similar to that reported in a recent study [8].

The LIPR values in Eq. (2) are plotted near the band edges for pristine and defective *a*-IGZO in Fig. 2, with the alignment of the Zn *d* bands. As discussed in Sec. II, the LIPR value of −0.7 is used to determine the mobility edges at which a transition occurs from localized to extended states. The VBM and CBM states are consistently determined by this way, regardless of whether an O_i interstitial exists in *a*-IGZO. The localized states near the band edges correspond to the tail states in the amorphous phase. The valence-band tail states are distributed up to 0.24 eV above

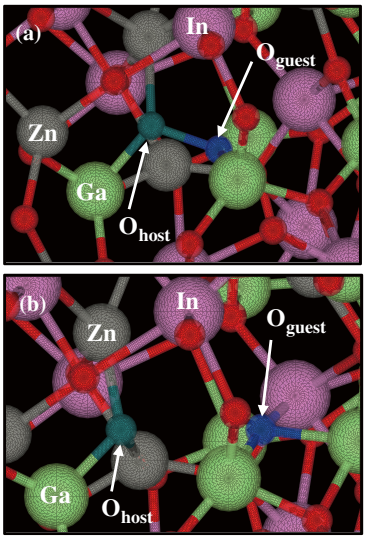

FIG. 1. The atomic structures of the O_i defect in the (a) neutral and (b) 2− charge states. Red balls denote the host O atoms which are not bonded to the guest O_i atom (blue), whereas a dark green ball represents the guest O atom forming the O—O dimer with the O_i atom.

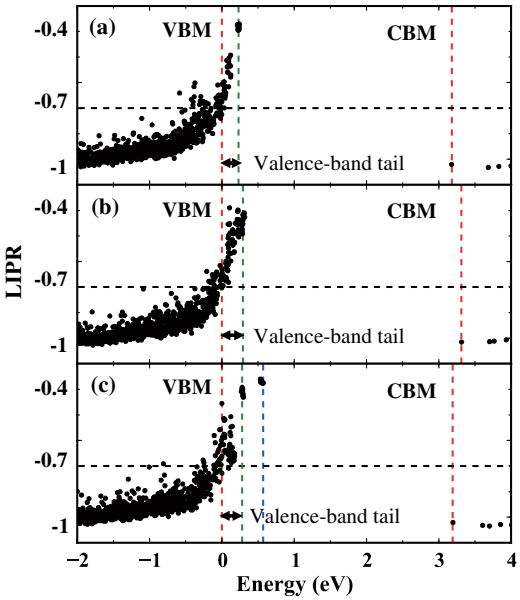

FIG. 2. The LIPR values are plotted as a function of energy for (a) pristine *a*-IGZO and defective *a*-IGZO with the O_i defects in the (b) neutral and (c) 2− charge states. The positions of the VBM and CBM states are denoted by red dashed lines. Green dashed lines represent the top of the valence-band tail, and a blue dashed line in (c) denotes the position of the localized nonbonding defect state of the O_i^{2-} defect, which is distinguished from the valence-band tail state.

the VBM in pristine *a*-IGZO, while their distribution is extended up to 0.55 eV in the presence of an O_i defect. On the other hand, no localized state appears near the conduction-band edge because the CBM state characterized by the cation *s* orbitals is less affected by disorder. Experimentally, the valence-band tail was estimated to be about 1.2 eV above the VBM, much larger than the conduction-band tail of about 20 meV below the CBM [30,35,36]. The calculated valence-band tail is smaller than the measured value, probably because the supercell size used is not sufficiently large enough to describe the degree of disorder. However, our approach based on the LIPR describes properly the dominant behavior of the valence-band tail over the conduction-band tail, similar to previous calculations [37].

For the neutral and 2− oxygen interstitials, which are denoted as O_i^0 and O_i^{2-}, respectively, the total density of states (DOS) and projected density of states (PDOS) onto the guest and its nearest host O atoms are plotted in Fig. 3. In the neutral state, the defect states of the O—O dimer are schematically drawn in Fig. 4. Because of the structural similarity between the O—O dimer and a free O_2 molecule, three bonding states represented by $pp\sigma$, $pp\pi(1)$, and $pp\pi(2)$ are positioned deep in the valence band. However, unlike the free O_2 molecule, the twofold degeneracy of the $pp\pi$ states is removed due to symmetry breaking by the nearest metal ions. In addition, since the O—O dimer interacts with the surrounding metal ions, the defect states are not exactly the same as those of the isolated O_2

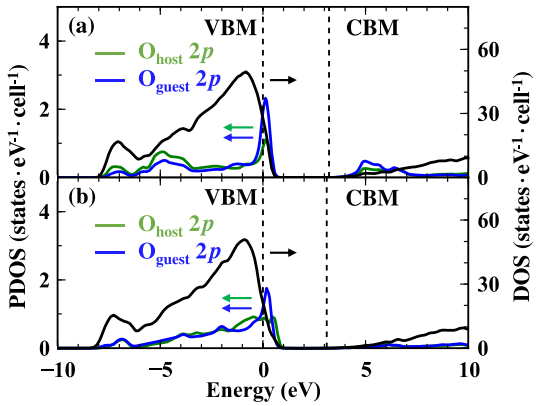

FIG. 3. The total DOS and PDOS onto the host (green) and guest (blue) O atoms in the (a) neutral and (b) 2− charge states, with the valence-band edge set to zero. The VBM and CBM states are determined by using the LIPR values.

molecule, with the twisted lobes pointing toward the neighboring cations. Among the antibonding states, the $pp\pi^*(1)$ and $pp\pi^*(2)$ states near the VBM are occupied by accepting electrons from the metal ions, whereas the $pp\sigma^*$ state in the conduction band is empty. In fact, the $pp\pi^*(1)$ state with the higher energy lies in the valence-band tail.

When the O—O dimer captures two electrons, the $pp\sigma^*$ state becomes filled, weakening the O—O dimer bond. As the O—O dimer is broken, the defect states of O_i^{2-} can be understood as the p-orbital states of an isolated O^{2-} atom. The filled $pp\sigma^*$ state is lowered and then turns to a new nonbonding defect state near the valence-band tail. In the broken-dimer configuration, we note that the 21 oxygen interstitials considered can be classified into two groups called A and B groups depending on the type of metal—O bonds around the broken dimer. Such a classification is

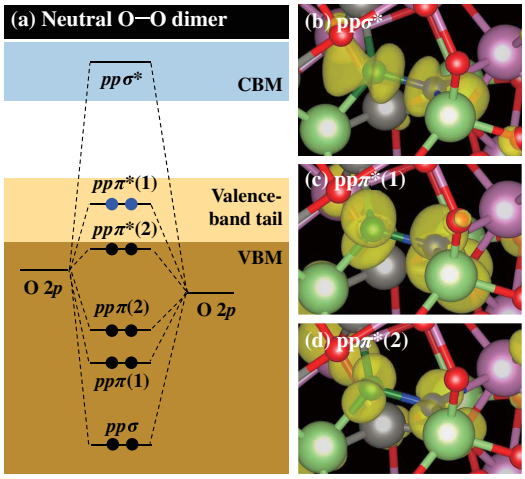

FIG. 4. (a) A schematic diagram for the energy levels of the bond orbitals in the neutral O—O dimer. Blue circles denote two electrons adopted from the surrounding metal ions. Isosurfaces of the charge densities for the (b) $pp\sigma^*$, (c) $pp\pi^*(1)$, and (d) $pp\pi^*(2)$ states.

closely related to the recovery of the dimer bond under light illumination, which we discuss later. The formation energies and bond lengths are similar for the neutral O—O dimers in both the groups. However, in the 2− state, there is a distinctive difference between the two groups. In group a, the broken dimer is surrounded with more Zn—O bonds than Ga—O bonds, with the average coordination number of 6.4. Thus, the O_i^{2-} interstitial is less separated from the host O atom, with the shorter interatomic distance, as compared to group B. In this case, the nonbonding state is more $pp\sigma^*$-like, with a defect level just above the valence-band tail. In group B, more Ga—O and In—O bonds are formed around the broken dimer, with the larger average coordination number of 7.1. Since the Ga—O bond is stronger than the Zn—O bond, the O_i^{2-} interstitials of type B become more stable, with the lower formation energy. Moreover, the nonbonding defect states in group B are relatively lower, lying in the valence-band tail or just below the VBM. Because of the strong Ga—O bond, the O—O dimer is more easily broken in the environment with more Ga atoms. This result is consistent with the experimental observation that a-IGZO exhibits a larger threshold-voltage shift as the Ga content increases [38].

B. O interstitial as an electron trap

The results of the GGA + U and HSE calculations for the average formation energies of O_i^0 and O_i^{2-} are shown and compared with those for an ionized V_O^{2+} defect in Fig. 5. When the $pp\sigma*$ state of the O—O dimer is lowered to the VBM in the 2− state, the energy difference between the two defect levels results in the energy gain. Since the

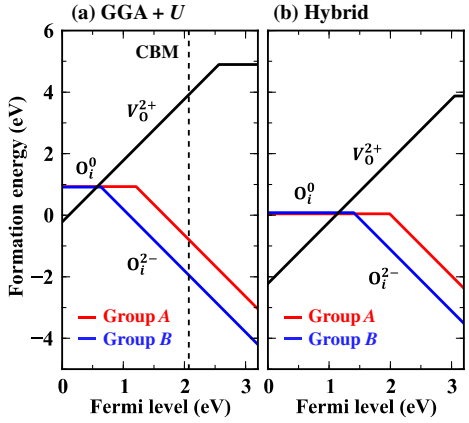

FIG. 5. The average formation energies of the O_i^0 and O_i^{2-} defects are compared with those for the V_O^{2+} defect under the extreme O-rich condition in the (a) GGA + U and (b) hybrid functional calculations. The dashed line denotes the GGA + U band gap of 2.07 eV with excluding the band tails for pristine a-IGZO, while the HSE band gap is 3.18 eV. Red and blue lines represent the O_i defects belonging to groups a and B, respectively. The average formation energies of the V_O^{2+} defect are taken from Ref. [6].

energy gain by two-electron capture is twice larger than for one-electron capture, the 2− charge state of O_i is more stable than the 1− charge state. In fact, the 1− charge state of O_i is found to be metastable, regardless of the position of the Fermi energy in the band gap. Thus, the O interstitial is a negative-U defect acting as a double acceptor. We find that the O_i defect is stabilized under O-rich conditions, while the V_O^{2+} defect is the dominant defect over the whole range of Fermi levels under O-poor conditions. The dependence of defect stability on the oxygen content is in good agreement with the experiments. In a-IGZO TFTs fabricated under different oxygen partial pressures, positive and negative V_{th} shifts have been observed for high and low oxygen contents, respectively [16,38]. Since the energetics of O-related defects depend on the growth condition, positive and negative V_{th} shifts caused by charge trapping under PBS and NBIS conditions are closely related to the O_i and V_O defects, which act as electron and hole traps, respectively.

In a-IGZO with high O contents, the O_i^{2-} defect becomes the dominant defect when the Fermi level is close to the CBM. As the Fermi level increases under positive gate bias stress, the O_i defect captures electrons and becomes the negatively charged defect. Thus, the excess O atoms deplete the channel region and thereby result in a positive V_{th} shift. The positive V_{th} shift is shown to vary with the thickness of active channel layers, exhibiting a larger shift for a thin layer [39]. Our result indicates that the charge trapping occurs more effectively in thin a-IGZO layers because oxygen in the ambient atmosphere easily penetrates into the active layer. In fact, the oxygen diffusivity in a-IGZO is found to be very high even at low temperatures, e.g., at 200 °C [40]. When the active channel is protected with passivation layers, the PBS instability can be improved due to the prevention of oxygen adsorption [11]. In general, the characteristics of a-IGZO TFTs are greatly improved by O_2 annealing or ozone (O_3) annealing at low temperatures below 250 °C due to the deficiency of V_O defects [41]. However, high-temperature O_3 annealing at 300 °C is shown to generate deep traps, thus, causing serious deterioration, which is attributed to the incorporation of excess O atoms.

We examine the capture process of electrons by the O_i defect. The capture barrier can be estimated from the configuration diagram in which the energies of the O_i defects in the neutral and 2− charge states are plotted as a function of the bond length of the O—O dimer, as shown in Fig. 6(a). For the 2− state, we examine the variation of the $pp\sigma^*$ state with the bond length of the O—O dimer and find the transition state where the $pp\sigma^*$ state crosses with the CBM [Fig. 6(b)]. The energy barrier for two-electron capture is estimated to be 0.33 eV by the GGA + U approach, while this value is significantly enhanced to 0.83 eV with the HSE functional. In previous HSE calculations, Nahm *et al.* [9] reported the similar energy

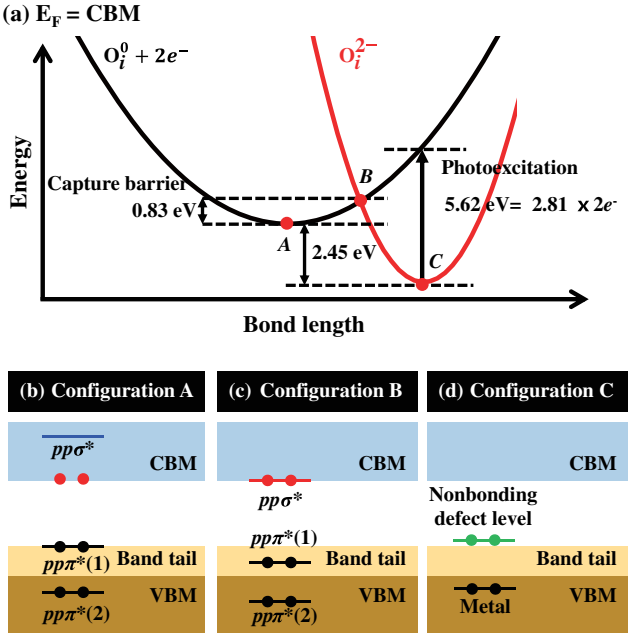

FIG. 6. (a) The configuration diagram for the formation energies of the O_i^0 and O_i^{2-} defects, which are obtained from the hybrid functional calculations for the Fermi level positioned at the CBM. In the neutral defect, two electrons are assumed to occupy the conduction-band-edge state. (b)–(d) The schematic diagrams of the defect states for three different bond lengths of the O—O dimer. The $pp\sigma^*$ state is lowered to the valence-band edge as the dimer bond length increases by capturing two electrons.

barrier of 0.9 eV for breaking an O—O dimer. However, they considered the O—O dimer which results from the disorder of host O atoms in a-IGZO with perfect stoichiometry. The HSE barrier for the electron capture is in good agreement with the measured values of 0.88 and 0.95 eV for as-grown and annealed samples, respectively [13]. Thus, it is inferred that the creation of the O_i^{2-} defect is responsible for the PBS instability.

For all the O_i defects considered, the calculated barriers (E_b) by the GGA + U approach are fitted by the method of least squares,

$$E_b = \alpha_0 + \sum_{i=\mathrm{In,Ga,Zn}} \alpha_i n_i, \tag{3}$$

where n_i (i = In, Ga, Zn) denotes the numbers of metal ions around the O—O dimer. The coefficients (in units of eV) are estimated to be $\alpha_0 = 0.61$, $\alpha_{In} = -0.004$, $\alpha_{Ga} = -0.1$, and $\alpha_{Zn} = -0.1$, with the R^2 value of 0.83. Because the formation energy at the transition state depends on interactions between the O—O dimer and the nearest metal ions, the energy barrier is closely related to the type and number of metal ions around the O—O dimer. As the In—O bond is weakest among the metal—O bonds, the energy barrier tends to increase if the

O—O dimer is surrounded with more In ions. This result suggests that the PBS instability can be mitigated with the high concentration of weak metal—O bonds, while adding Ga atoms is shown to improve the stability under the NBIS condition [6].

C. Effects of light-illumination and negative-bias stress

When the O_i^{2-} interstitial is photoexcited, the $pp\sigma^*$-like nonbonding state near the valence-band tail is significantly affected by releasing two electrons. For the O_i defects in group *a*, the average position of the $pp\sigma^*$-like localized levels is estimated to be 0.75 eV above the VBM in the GGA + *U* approach. With the hybrid functional, the average defect level of O_i^{2-} is positioned at 0.64 eV above the VBM, while this level becomes lower for group *B* lying near the VBM, as shown in Fig. 7. Under light-illumination or negative-bias stress, the O_i^{2-} defect captures hole carriers so that the O_i defect recovers the O—O dimer configuration. Once the neutral O—O dimer is reformed, the device stability is restored, with a negative shift of $V_{\rm th}$ to its original threshold-voltage position. The photon energy to recover the dimer state depends on the type of the O_i defect. In group *a*, since the defect state of O_i^{2-} lies above the valence-band tail, this defect responds to light illumination with photon energies larger than 2.54 eV. On the other hand, in group *B*, larger photon energies are required for photoexcitation due to the deeper defect levels. These results agree well with the experimental observation that the transfer characteristics of *a*-IGZO TFTs are recovered by light illumination with the photon energies ≥ 2.3 eV, which is smaller than the band gap [41].

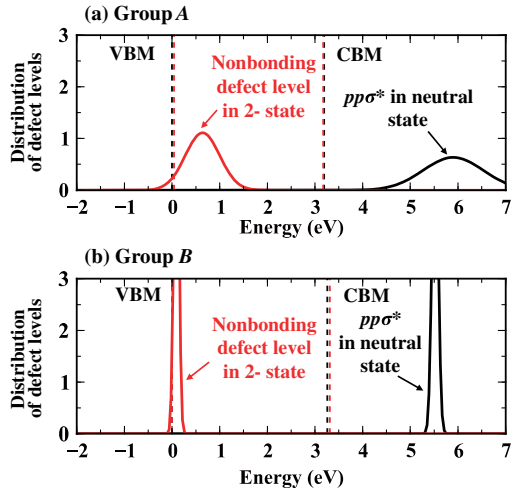

FIG. 7. The distributions of the $pp\sigma^*$ states of the O_i^0 defects and the nonbonding defect levels of the O_i^{2-} defects, which are obtained from the hybrid functional calculations for the defects belonging to groups *A* and *B*. Gaussian distribution functions are used to visualize the distribution of the defect levels. In each distribution, the peak and width represent the average value and standard deviation of the defect levels, respectively, with the area normalized to 1.

As a gate bias changes from positive to negative in *a*-IGZO, the threshold voltage is shown to shift negatively to its original position [4]. The effect of negative-bias stress (NBS) is also explained by the hole capture of O_i^{2-}. When holes are generated by applying a negative gate voltage, they can be captured by the O_i^{2-} defects, regardless of whether the defect level is positioned above or near the VBM. Since the Fermi level shifts to the VBM under NBS, the neutral O—O dimer configuration can be recovered without any energy barrier. We confirm that the broken-dimer configuration easily relaxes to the dimer state for the defects in group *a*. However, the recovery of the dimer state cannot be confirmed for group *B*, because it is difficult to remove electrons from the defect level which lies inside the valence-band tail. Nevertheless, we expect that the recovery of the dimer state occurs either under light illumination or NBS, regardless of the defect type.

IV. CONCLUSIONS

We investigate the atomic and electronic properties of O interstitial defects in *a*-IGZO by performing the hybrid density-functional calculations. We find that the O—O dimer, which is the most stable configuration in the neutral state, undergoes outward relaxations upon electron capture and is eventually broken. When the Fermi level is close to the conduction-band edge, the stability of the broken dimer in the 2− charge state is attributed to the large shift of the antibonding defect level toward the valence-band edge. Our result indicates that the O interstitial defects act as electron traps in the channel region of oxide TFTs, in good agreement with the experimental finding that O-rich *a*-IGZO samples are more affected under positive-bias stress, as compared to negative-bias illumination stress. While the energy barrier is about 0.83 eV for the electron capture by the O—O dimer, the ionized broken dimer easily recovers its original dimer configuration upon photoexcitation, without the energy barrier.

ACKNOWLEDGMENTS

This work is supported by the National Research Foundation of Korea under Grant No. NRF-2005-0093845 and by the Supercomputing Center and Korea Institute of Science and Technology Information with supercomputing resources including technical support (Grant No. KSC-2014-C1-039).

[1] T. Kamiya, K. Nomura, and H. Hosono, Origins of high mobility and low operation voltage of amorphous oxide TFTs: Electronic structure, electron transport, defects and doping, J. Disp. Technol. **5**, 273 (2009).

[2] K. Nomura, H. Ohta, A. Takagi, T. Kamiya, M. Hirano, and H. Hosono, Room-temperature fabrication of transparent exible thin-film transistors using amorphous oxide semiconductors., Nature (London) **432**, 488 (2004).
[3] K. Takechi, M. Nakata, T. Eguchi, H. Yamaguchi, and S. Kaneko, Comparison of ultraviolet photo-field effects between hydrogenated amorphous silicon and amorphous $InGaZnO_4$ thin-film transistors, Jpn. J. Appl. Phys. **48**, 010203 (2009).
[4] S. Park, E. N. Cho, and I. Yun, Instability of light illumination stress on amorphous In-Ga-Zn-O thin-film transistors, J. Soc. Inf. Disp. **21**, 333 (2013).
[5] K.-H. Lee, J. S. Jung, K. S. Son, J. S. Park, T. S. Kim, R. Choi, J. K. Jeong, J.-Y. Kwon, B. Koo, and S. Lee, The effect of moisture on the photon-enhanced negative bias thermal instability in Ga-In-Zn-O thin film transistors, Appl. Phys. Lett. **95**, 232106 (2009).
[6] H.-K. Noh, K. J. Chang, B. Ryu, and W.-J. Lee, Electronic structure of oxygen-vacancy defects in amorphous In-Ga-Zn-O semiconductors, Phys. Rev. B **84**, 115205 (2011).
[7] B. Ryu, H.-K. Noh, E.-A. Choi, and K. J. Chang, O-vacancy as the origin of negative bias illumination stress instability in amorphous In-Ga-Zn-O thin film transistors, Appl. Phys. Lett. **97**, 022108 (2010).
[8] J. Robertson and Y. Guo, Light induced instability mechanism in amorphous InGaZn oxide semiconductors, Appl. Phys. Lett. **104**, 162102 (2014).
[9] H.-H. Nahm, Y.-S. Kim, and D. H. Kim, Instability of amorphous oxide semiconductors via carrier-mediated structural transition between disorder and peroxide state, Phys. Status Solidi B **249**, 1277 (2012).
[10] A. Suresh and J. F. Muth, Bias stress stability of indium gallium zinc oxide channel based transparent thin film transistors, Appl. Phys. Lett. **92**, 033502 (2008).
[11] J. K. Jeong, H. Won Yang, J. H. Jeong, Y.-G. Mo, and H. D. Kim, Origin of threshold voltage instability in indium-gallium-zinc oxide thin film transistors, Appl. Phys. Lett. **93**, 123508 (2008).
[12] J.-M. Lee, I.-T. Cho, J.-H. Lee, and H.-I. Kwon, Bias-stress-induced stretched-exponential time dependence of threshold voltage shift in InGaZnO thin film transistors, Appl. Phys. Lett. **93**, 093504 (2008).
[13] M. D. H. Chowdhury, P. Migliorato, and J. Jang, Time-temperature dependence of positive gate bias stress and recovery in amorphous indium-gallium-zinc-oxide thin-film-transistors, Appl. Phys. Lett. **98**, 153511 (2011).
[14] J. Lee, J.-S. Park, Y. S. Pyo, D. B. Lee, E. H. Kim, D. Stryakhilev, T. W. Kim, D. U. Jin, and Y.-G. Mo, The influence of the gate dielectrics on threshold voltage instability in amorphous indium-gallium-zinc oxide thin film transistors, Appl. Phys. Lett. **95**, 123502 (2009).
[15] M. E. Lopes, H. L. Gomes, M. C. R. Medeiros, P. Barquinha, L. Pereira, E. Fortunato, R. Martins, and I. Ferreira, Gate-bias stress in amorphous oxide semiconductors thin-film transistors, Appl. Phys. Lett. **95**, 063502 (2009).
[16] W.-T. Chen, S.-Y. Lo, S.-C. Kao, H.-W. Zan, C.-C. Tsai, J.-H. Lin, C.-H. Fang, and C.-C. Lee, Oxygen-dependent instability and annealing/passivation effects in amorphous In-Ga-Zn-O thin-film transistors, IEEE Electron Device Lett. **32**, 1552 (2011).
[17] H. Oh, S.-M. Yoon, M. K. Ryu, C.-S. Hwang, S. Yang, and S.-H. K. Park, Photon-accelerated negative bias instability involving subgap states creation in amorphous In-Ga-Zn-O thin film transistor, Appl. Phys. Lett. **97**, 183502 (2010).
[18] K. H. Ji, J.-I. Kim, H. Y. Jung, S. Y. Park, R. Choi, U. K. Kim, C. S. Hwang, D. Lee, H. Hwang, and J. K. Jeong, Effect of high-pressure oxygen annealing on negative bias illumination stress-induced instability of InGaZnO thin film transistors, Appl. Phys. Lett. **98**, 103509 (2011).
[19] C. Freysoldt, B. Grabowski, T. Hickel, J. Neugebauer, G. Kresse, A. Janotti, and C. G. Van de Walle, First-principles calculations for point defects in solids, Rev. Mod. Phys. **86**, 253 (2014).
[20] J. Heyd, G. E. Scuseria, and M. Ernzerhof, Hybrid functionals based on a screened Coulomb potential, J. Chem. Phys. **118**, 8207 (2003).
[21] J. Heyd, G. E. Scuseria, and M. Ernzerhof, Erratum: Hybrid functionals based on a screened Coulomb potential, J. Chem. Phys. **118**, 8207 (2003); **124**, 219906 (2006).
[22] J. P. Perdew and Y. Wang, Accurate and simple analytic representation of the electron-gas correlation energy, Phys. Rev. B **45**, 13244 (1992).
[23] P. E. Blöchl, Projector augmented-wave method, Phys. Rev. B **50**, 17953 (1994).
[24] G. Kresse and J. Furthüller, Efficient iterative schemes for *ab initio* total-energy calculations using a plane-wave basis set, Phys. Rev. B **54**, 11169 (1996).
[25] K. Nomura, T. Kamiya, H. Ohta, T. Uruga, M. Hirano, and H. Hosono, Local coordination structure and electronic structure of the large electron mobility amorphous oxide semiconductor In-Ga-Zn-O: Experiment and *ab initio* calculations, Phys. Rev. B **75**, 035212 (2007).
[26] D.-Y. Cho, J. Song, K. D. Na, C. S. Hwang, J. H. Jeong, J. K. Jeong, and Y.-G. Mo, Local structure and conduction mechanism in amorphous In-Ga-Zn-O films, Appl. Phys. Lett. **94**, 112112 (2009).
[27] S. L. Dudarev, G. A. Botton, S. Y. Savrasov, C. J. Humphreys, and A. P. Sutton, Electronenergy loss spectra and the structural stability of nickel oxide: An LSDA + U study, Phys. Rev. B **57**, 1505 (1998).
[28] C. McGuinness, C. B. Stagarescu, P. J. Ryan, J. E. Downes, D. Fu, K. E. Smith, and R. G. Egdell, Influence of shallow core-level hybridization on the electronic structure of post-transition metal oxides studied using soft x-ray emission and absorption, Phys. Rev. B **68**, 165104 (2003).
[29] E. A. Albanesi, S. J. Sferco, I. Lefebvre, G. Allan, and G. Hollinger, Electronic structure of binary and ternary Ga or As oxides, Phys. Rev. B **46**, 13260 (1992).
[30] K. Nomura, T. Kamiya, H. Yanagi, E. Ikenaga, K. Yang, K. Kobayashi, M. Hirano, and H. Hosono, Subgap states in transparent amorphous oxide semiconductor, In-Ga-Zn-O, observed by bulk sensitive x-ray photoelectron spectroscopy, Appl. Phys. Lett. **92**, 202117 (2008).
[31] G. G. Naumis, Internal mobility edge in doped graphene: Frustration in a renormalized lattice, Phys. Rev. B **76**, 153403 (2007).

[32] H. Omura, H. Kumomi, K. Nomura, T. Kamiya, M. Hirano, and H. Hosono, First-principles study of native point defects in crystalline indium gallium zinc oxide, J. Appl. Phys. **105**, 093712 (2009).

[33] S. Limpijumnong, X. Li, S.-H. Wei, and S. B. Zhang, Substitutional diatomic molecules NO, NC, CO, N_2, and O_2: Their vibrational frequencies and effects on *p* doping of ZnO, Appl. Phys. Lett. **86**, 211910 (2005).

[34] A. Janotti and C. G. Van de Walle, Native point defects in ZnO, Phys. Rev. B **76**, 165202 (2007).

[35] J. H. Kim, U. K. Kim, Y. J. Chung, and C. S. Hwang, Correlation of the change in transfer characteristics with the interfacial trap densities of amorphous In-Ga-Zn-O thin film transistors under light illumination, Appl. Phys. Lett. **98**, 232102 (2011).

[36] S. Lee and A. Nathan, Localized tail state distribution in amorphous oxide transistors deduced from low temperature measurements, Appl. Phys. Lett. **101**, 113502 (2012).

[37] Y. Kang, Y. Cho, and S. Han, Cation disorder as the major electron scattering source in crystalline InGaZnO, Appl. Phys. Lett. **102**, 152104 (2013).

[38] P. Barquinha, L. Pereira, G. Gonçalves, R. Martins, and E. Fortunato, Toward high performance amorphous GIZO TFTs, J. Electrochem. Soc. **156**, H161 (2009).

[39] J. Jeong, G. J. Lee, J. Kim, J. Kim, and B. Choi, Oxygen dispersive diffusion induced bias stress instability in thin active layer amorphous In-Ga-Zn-O thin-film transistors, Appl. Phys. Express **6**, 031101 (2013).

[40] K. Watanabe, D.-H. Lee, I. Sakaguchi, K. Nomura, T. Kamiya, H. Haneda, H. Hosono, and N. Ohashi, Surface reactivity and oxygen migration in amorphous indium-gallium-zinc oxide films annealed in humid atmosphere, Appl. Phys. Lett. **103**, 201904 (2013).

[41] K. Ide, Y. Kikuchi, K. Nomura, M. Kimura, T. Kamiya, and H. Hosono, Effects of excess oxygen on operation characteristics of amorphous In-Ga-Zn-O thin-film transistors, Appl. Phys. Lett. **99**, 093507 (2011).